

Solar wind coupling to and predictability of ground magnetic fields and their time derivatives

R. S. Weigel

National Research Council, NASA Goddard Space Flight Center, Greenbelt, Maryland, USA

A. J. Klimas

NASA Goddard Space Flight Center, Greenbelt, Maryland, USA

D. Vassiliadis

Universities Space Research Association, Seabrook, Maryland, USA

Received 2 August 2002; revised 23 January 2003; accepted 18 March 2003; published 23 July 2003.

[1] A spatial and dynamic study of solar wind driving of high-latitude ground magnetic fields and their time derivatives is given. Nonlinear, data-derived basis functions are used to determine the optimal solar wind driven dynamic coupling function at high-latitude locations. The method does not assume a solar wind driving function a priori so that an unbiased determination of the relative influence of different driving processes can be made. Using this method, the locations where high-latitude models capture signatures of different driving processes, such as reconnection and the Kelvin-Helmholtz instability, are revealed for both the amplitude of the field and its time derivative. The time rate of change of the field is a disturbance measure related to geomagnetically induced currents. For the amplitude of the ground magnetic field the primary driver is reconnection; the time rate of change of the field has signatures of both reconnection driving in the nightside sector and Kelvin-Helmholtz driving in the prenoon sector. The independent influence of the solar wind ion density and azimuthal component of the magnetic field in driving magnetic field fluctuations is found to be small at auroral-zone latitudes. The data-derived coupling functions are also used to estimate the expected prediction error of a general class of models that specify the ground magnetic field or its time derivative given solar wind plasma measurements. Prediction efficiencies as small as zero and as large as 0.7 for both the amplitude of the field and its time derivative are possible. The prediction efficiency is highly dependent on spatial location and the direction of field being predicted. **INDEX TERMS:** 2447 Ionosphere: Modeling and forecasting; 2409 Ionosphere: Current systems (2708); 2784 Magnetospheric Physics: Solar wind/magnetosphere interactions; 2722 Magnetospheric Physics: Forecasting; **KEYWORDS:** solar-wind driving, geomagnetic fields, geomagnetically induced currents, predictability, fluctuations

Citation: Weigel, R. S., A. J. Klimas, and D. Vassiliadis, Solar wind coupling to and predictability of ground magnetic fields and their time derivatives, *J. Geophys. Res.*, 108(A7), 1298, doi:10.1029/2002JA009627, 2003.

1. Introduction

[2] A classic problem in space plasma physics centers on how the solar wind couples to Earth's ionosphere and how it generates the large scale dynamics of ground magnetic fields at high latitudes. Early models of this coupling used a linear filter approach to model the dynamics of global geomagnetic indices such as AE and AL [Clauer *et al.*, 1981]. More recent works dealt with nonlinear generalizations of a linear filter to specify AE and AL [Vassiliadis *et al.*, 1995]; [Klimas *et al.*, 1997, 1999]. Physics-based

nonlinear models that explicitly incorporated a storage unloading mechanism, which could account for the bimodal feature in the impulse response functions computed by Bargatze *et al.* [1985], were later introduced [Klimas *et al.*, 1992, 1994, 1996; Horton and Doxas, 1996, 1998]. Other models incorporated a nonlinearity in the parameters of a linear system of ordinary differential equations [Rostoker and Pascal, 1990]. All of these models specify the overall level of geomagnetic activity, as measured by a global activity index, given the state of the solar wind.

[3] Later, models with higher spatial resolution than that of a geomagnetic index were introduced. These models generally use an empirical or statistical approach to prescribe either the time evolution of ground magnetic fields or

to determine global patterns of the electric field and potential under different solar wind conditions. Such models include the Assimilative Mapping of Ionospheric Electrodynamics (AMIE) [Richmond and Kamide, 1988], IZMIRAN Electrodynamics Model (IZMEM) [Papitashvili et al., 1994] and Linear Modeling of Ionospheric Electrodynamics (LiMIE) [Papitashvili et al., 1998]. When used in a predictive mode, these models can specify the future state of a geomagnetic or electrodynamic quantity (or pattern) as a function of prior solar wind measurements. Not all high-latitude models directly specify the ground magnetic field. For example, the Weimer [1995], Weimer [1996], and Heppner and Maynard [1987] models give the high-latitude electric-field pattern directly from satellite measurements, from which the ground magnetic field can then be computed. Global MHD models can also be used to specify local geomagnetic activity. In this case the mapping of solar wind quantities is specified by the time evolution of the MHD equations given the initial magnetospheric state and solar wind conditions at the magnetosphere boundary [Fedder et al., 1995; Winglee et al., 1997].

[4] Studies of these high-latitude models usually focus on high-latitude electric field and convection patterns that are statistically specified given the solar wind state (e.g., orientation of B^{IMF} , magnitude of solar wind speed). As the possibility of using such models for real-time prediction nears, it becomes necessary to estimate the inherent uncertainty in the prediction of high-latitude disturbances given solar wind information. The results presented in this paper concern the data-model correlation of a model that is a generalized form of the above-described high-latitude models. Besides computing the expected prediction performance (data-model correlation), we use the developed method to determine how strongly a given high-latitude location is coupled to the solar wind and what the form of the optimal driving function is.

[5] The focus of this paper is on determining both the form of the coupling function and the prediction error of a generalized nonlinear statistical filter that specifies the ground magnetic field given the solar wind state (from a single upstream monitor) from which the following questions can be answered: (1) How closely can the ground magnetic field and its time derivative be predicted at a high-latitude location given only measurements from a single location in the upstream solar wind (i.e., what is the expected level of prediction or data-model correlation)?, (2) Which solar wind variables give the most information about the state of the field at a given location?, and (3) How does the form of the solar wind driver, or optimal coupling function, change as a function of spatial location?

[6] To answer questions 1–3, a very general coupling function is needed. A neural network function has the property that it can produce nearly any continuous input-output mapping function [Cybenko, 1989]. We use this form of mapping to create nonlinear data-derived models that can be used to answer questions 1–3 quantitatively. This approach allows an input of a separate time history of each solar wind variable to be used because the output can be nearly any function of the input variables. It has the advantage of allowing for nonlinearities and allowing the form of the driving function to be unspecified; the coupling function is determined directly from the data. This approach

is a nonlinear generalization of high-dimensional moving average filters [Box and Jenkins, 1976]. Neural network mapping functions have been described and employed on geomagnetic indices [Gleisner and Lundstedt, 1997; Weigel et al., 1999; Wu and Lundstedt, 1997; Takalo and Timonen, 1997; Gavrishchaka and Ganguli, 2001] and on an auroral-zone magnetometer data [Gleisner and Lundstedt, 2001; Weigel et al., 2002].

[7] The advantage of the data-derived approach with an unconstrained coupling function is the optimal coupling function is determined directly from the data, and any variable whose contribution is not statistically significant can be eliminated. Also, because the mapping function can take on many nonlinear forms, the litany of proposed coupling functions does not have to be tested (see Baker [1986] for summary of proposed functions).

[8] Besides revealing information about the form of the coupling function, the prediction error (or data-model correlation) highlights the locations where predictive models are expected to produce good or poor results if only the solar wind state is known. The prediction error results can also be used to explain differences in model predictions of high-latitude disturbances. For example, Winglee et al. [1997] notes that estimates of the cross polar-cap potential of several high-latitude electric field models can differ by factors on the order of two; Ridley et al. [2000] shows an event for which the error in cross-polar cap potential derived from a real-time AMIE (SAMIE or rtAMIE) model is time-dependent and that the error in electric field has a spatial dependence. Because the prediction error is a measure of uncertainty, the results of the generalized high-latitude model presented here can be used to explain the differences between models.

[9] The coupling of the solar wind to $|dB_x/dt|$, the absolute value time rate of change of the north-south component of the ground magnetic field, has been considered by Weigel et al. [2002]. Here we extend this work to include both the magnitude of the field for three components of the ground magnetic field, B_x , B_y , and $B_H = (B_x^2 + B_y^2)^{1/2}$, and their time derivatives. At auroral-zone latitudes, B_x is primarily a measure of the amplitude of eastward and westward flowing currents in the ionosphere. The time rate of change of B_x implies the existence of an inductive electric field; the time rate of change is important because it describes the variability or volatility of ionospheric currents and can be used to estimate geomagnetically induced currents [Pirjola and Viljanen, 1998; Boteler et al., 2000].

[10] The time scale considered is based on 30-min averages of B_i and $|dB_i/dt|$ ($i = x, y$ or H) derived from 1-min data. This averaging interval is small enough to allow for an approximately 30-min prediction lead time for a satellite 60 min upstream of Earth yet is long enough to allow for computations to be performed on a 2-year data set. Moreover, a 30-min lead time is consistent with the uncertainty of at least ± 15 min in the time of propagation of a solar wind structure from the $L1$ point to Earth [Kelly et al., 1986].

[11] Optimal coupling functions for B_i and $|dB_i/dt|$ are found by a direct mapping of only solar wind data. The fluctuation amplitude $|dB_i/dt|$ is predicted directly from its own mapping function; this is in contrast to an algorithm that would use a prediction of B_i to compute $|dB_i/dt|$. The direct approach is used because a model optimized to specify B_i

Table 1. Coordinates of IMAGE Magnetometer Stations Used in This Study^a

Station	Geographic Lat.	Geographic Long.	CGM Lat.	CGM Long.	MLTMN
NAL	78.92	11.95	76.14	111.90	2050
LYR	78.20	15.82	75.19	112.72	2046
HOR	77.00	15.60	74.08	110.18	2055
HOP	76.51	25.01	72.99	115.65	2033
BJN	74.50	19.20	71.40	108.57	2100
SOR	70.54	22.22	67.30	106.58	2107
ABK	68.35	18.82	65.27	102.13	2125
KIR	67.84	20.42	64.66	103.00	2122
SOD	67.37	26.63	63.87	107.61	2103
OIJ	64.52	27.23	60.94	106.45	2107
HAN	62.30	26.65	58.67	104.90	2113
NUR	60.50	24.65	56.86	102.44	2123

^aThe CGM coordinates were obtained using the IGRF model for year 1999. MLTMN is the UT when the station has a magnetic local time of midnight.

will rarely produce optimal predictions of $|dB_i/dt|$. The developed models are used to extract information about solar wind processes that drive geomagnetic disturbances. For this reason, previous values of the geomagnetic field are not included as model inputs, although they may increase the prediction efficiency without decreasing the lead time.

2. Method

[12] The data set used for this study consists of ground magnetometer measurements at 1-min resolution from the 12 IMAGE stations [Luhr *et al.*, 1998] listed in Table 1 for days 23–365 of 1998 and all days of 1999. The solar wind magnetic field data [Smith *et al.*, 1988] is from the ACE satellite located, on average, 62 min upstream of Earth. The field data (in GSM coordinates) were interpolated from 16-s averages to a 1-min time grid. The solar wind ion velocity data [McComas *et al.*, 1998] were interpolated from 64-s averages to a 1-min time grid.

[13] Two measures of the ionospheric disturbance level are considered: the amplitudes of the geographic component of the ground magnetic field, B_i ($i = x, y$ or H), and the absolute value of its time derivative averaged over 30 min. The disturbance D ($= B_i$ or $|dB_i/dt|$) at a magnetometer with latitude m is the block average with window width $t_a = 30$ min

$$D_{LT}^m(t) = \frac{1}{t_a} \sum_{j=t-\frac{t_a}{2}}^{t+\frac{t_a}{2}-1} B_i(j) \quad \text{or} \quad (1)$$

$$D_{LT}^m(t) = \frac{1}{t_a} \sum_{j=t-\frac{t_a}{2}}^{t+\frac{t_a}{2}-1} \left| \frac{\Delta B_i(j)}{\Delta t} \right|, \quad (2)$$

where $\Delta t = t(j) - t(j-1) = 1$ min, $\Delta B_i = B_i(j) - B_i(j-1)$, and LT is the local time of magnetometer m at universal time t . Note that the prediction lead time of $t_d - 30$ min is variable, where t_d is the time it takes the solar wind to travel from ACE to the magnetopause (the communication time from the satellite to Earth is small and ignored). For this data set the average delay time, t_d , is 62 min and the minimum is 30 min, giving prediction lead times of 32 min and 0 min, respectively.

[14] The data-derived coupling functions that map the solar wind information to B_i and $|dB_i/dt|$ are determined using an input vector containing only solar wind data. Measurements of the ground magnetic field are not used to specify its future state. If measurements of recent ground magnetic fields are used, predictions will be improved, but the lead time is reduced if measurements are used from time intervals less than $t_d - 30$ min.

[15] To allow for a spatial dependence in the coupling function, a different mapping function is generated for 48 local times and at each magnetometer latitude, m . The predicted disturbance \mathcal{D} in the interval centered on time t is approximated by a nonlinear mapping of 3.0 hours of time-delayed solar wind data

$$\mathcal{D}_{LT}^m(t) = f_{LT}^m([\mathbf{I}(t - t_d), \mathbf{I}(t - t_d - t_a), \dots, \mathbf{I}(t - t_d - 5t_a)]), \quad (3)$$

where $LT = [0, 0.5, \dots, 23.5]$ hour. The LT resolution of the mapping function can be as small low as 1 min, but a 30-min LT resolution is small enough for a linear interpolation of f in LT to be accurate. The resolution in m is limited by the spacing of the magnetometers in latitude. The parameters of the mapping function f are determined by minimizing the error between the measured disturbance D_{LT}^m and the predicted disturbance \mathcal{D}_{LT}^m on the days of the training set (the in-sample data). The model of equation (3) specifies \mathcal{D} at any time t . Thus it can specify the disturbance at a LT not equal to that of the magnetometer at that latitude. Although we do not have a continuous sampling at a fixed local time, such a sampling is effectively generated by using a many-day time series [Valdivia *et al.*, 1999]. A schematic of the mapping method is shown in Figure 1.

[16] The solar wind plasma measurements used as inputs to f

$$\mathbf{I}(t) = [\rho_i(t), B_y^{\text{IMF}}(t), B_z^{\text{IMF}}(t), v_x(t)] \quad (4)$$

are averaged over an interval of t_a centered on time t . The data are left in their original form and is not combined into a coupling function such as the cross-tail electric field $v_x B_s^{\text{IMF}}$ or the ϵ parameter [Akasofu, 1979]. This allows the appropriate coupling function to be determined by the data-derived mapping function, which has these forms as possible solutions. For example, a possible solution for $D = B_x$ at auroral zone latitudes in the LT range of [23, 3] is

$$f_{LT=[23,3]} \simeq v_x B_s^{\text{IMF}}, \quad (5)$$

which is expected from studies of AL - $v_x B_s^{\text{IMF}}$ coupling because most of the contribution to AL is from the north-south component of the field, B_x , in the local time range [2300, 0300] [Allen and Kroehl, 1975]. At higher latitudes, the B_z^{IMF} dependence of f_{LT} should take on a piecewise linear form [Troshichev and Gusev, 1994], which can be written in terms of two slope parameters, s^+ and s^- ,

$$f_{LT} = s_{LT}^+ (B_z^{\text{IMF}} + |B_z^{\text{IMF}}|) + s_{LT}^- (|B_z^{\text{IMF}}| - B_z^{\text{IMF}}). \quad (6)$$

Because the “hard-rectifier” B_z^{IMF} dependence of equation (5) is the case of $s^+ = 0$, a gradual increase in s^+ from auroral zone to high-latitude locations is expected.

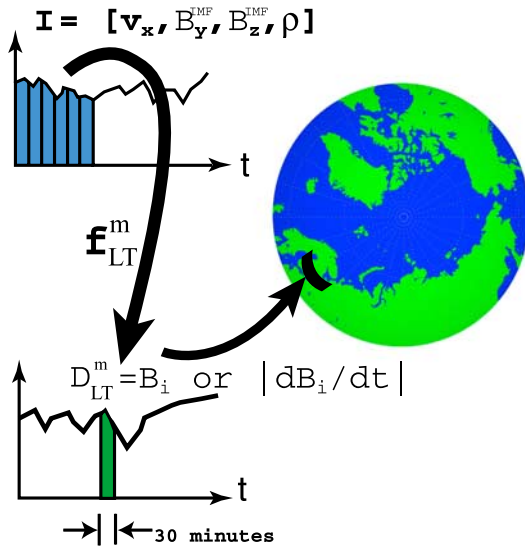


Figure 1. Schematic of mapping procedure. The mapping function f takes input \mathbf{I} which contains 30-min averages of solar wind data over the previous 3.0 hours and specifies the 30-min average disturbance level D at local time LT at the latitude of magnetometer, m . A different mapping function is determined for each disturbance measure so that $|dB_i/dt|$ is directly predicted, as opposed to being calculated from B_i . The solar wind inputs are not precombined into a coupling function so that any LT or m dependence of the form of f can be detected.

[17] The measure of coupling, or predictability, is the prediction efficiency [Detman and Vassiliadis, 1997],

$$PE_{LT}^m = 1 - \frac{E_{LT}^m}{\sigma_D^2}. \quad (7)$$

The notation $PE(D_{LT}^m; \mathbf{I} = [V_1, V_2, \dots])$ is used to represent the out-of-sample prediction efficiency for disturbance measure D by a model with coefficients derived using six time-delayed copies of $\mathbf{I} = [V_1, V_2, \dots]$ as the input vector. The error at magnetometer m is

$$E_{LT}^m = \left\langle (D_{LT}^m(T) - \mathcal{D}_{LT}^m(T))^2 \right\rangle, \quad (8)$$

where T is the day number, and the average is taken over the days of the test set (the out-of-sample data). Thus the prediction error for a magnetometer at each of the 48 local times is determined by averaging over the common local times from the days of the test set. The PE is the fraction of the variance in the data, D , at local time LT that is predicted by \mathcal{D} .

[18] A prediction efficiency of zero indicates that the prediction is as good as a model that uses only the average value of D as a predictor. The PE is related to the square of the correlation coefficient, R , by $PE = R^2$ if both the mean and standard deviation of both the predicted and measured value are equal and the prediction error is uncorrelated with the prediction. For this data set, the equality generally holds when the PE is greater than 0.10.

[19] To eliminate any bias due to the choice of days used for the training and test set, we use a random sample of half

of the days of the data set for the training set; the remaining days are used as the test set. All PE values reported are averages from the test-set error for 20 different random choices of training and test sets. This averaging serves to eliminate any bias that would occur if, for example, an exceptional number of days in the training set were quiet days while the test set contained mostly disturbed days. Any seasonal dependence is removed, although ideally the mapping function would be dependent on season, especially for the higher latitude locations [Troshichev and Voloshinov, 1988; Vennerstrom et al., 1991]. For this analysis the PE is interpreted as the fraction of the measured disturbance at $[m, LT]$ that can be derived from the solar wind using an out-of-sample data set.

[20] Because the PE from the out-of-sample data can take on negative values, the average of the 20 different trials will often yield a PE that is less than the average of 20 corresponding R^2 values. We prefer the PE error measure because positive values of the PE can always be interpreted as the fraction of the variance of the data that the model produces (whereas for R^2 this only holds for the conditions described above). In addition, negative values of PE work to exaggerate locations where the model has poor generalization (i.e., where the model has much better in-sample performance than out-of-sample performance).

[21] The PE values are computed using an out-of-sample data set. Because 20 different trials were performed, the out-of-sample data will contain days that occurred prior to some of the days of the training data. This would not be possible in a real-time prediction application. However, trials in which the time ordering was preserved (the training set is the first year of data, test set is the second year) have results that are consistent with what is presented here.

[22] We use a feed-forward neural network as the non-linear mapping function f because it can approximate almost any [Cybenko, 1989] continuous input-output mapping. The mapping function f for each magnetometer is a neural network in the form of a multilayer perceptron [Bishop, 1995]

$$f(\mathbf{X}) = \sum_{i=1}^M W_i \sum_{j=1}^N \tanh(w_{ij}X_j + a_i) + W_0. \quad (9)$$

In the limit of $w_{ij}X_j + a_i \ll 1$ for all ij the mapping is a linear moving average filter similar to those used in models which predict the amplitude of the ground magnetic field, \mathbf{B} [Papitashvili et al., 1994]. The $M(N+2)+1$ weights are determined using the scaled conjugate gradient descent minimization method with the input-output vectors of the training set. The number of weights of the input layer N is fixed by the dimension of the input vector, \mathbf{X} . The number of weights in the hidden layer M is chosen to be 3; the results are insensitive to changes in this number.

3. Average Levels of Disturbance

[23] Before considering solar wind coupling to and average prediction error of geomagnetic disturbances as a function of spatial location, it is instructive to view some of the statistical properties of the measurements that are being modeled. In Figure 2, 15-day segments of B_x and dB_x/dt from 1998 are shown for both a lower polar cap magnetom-

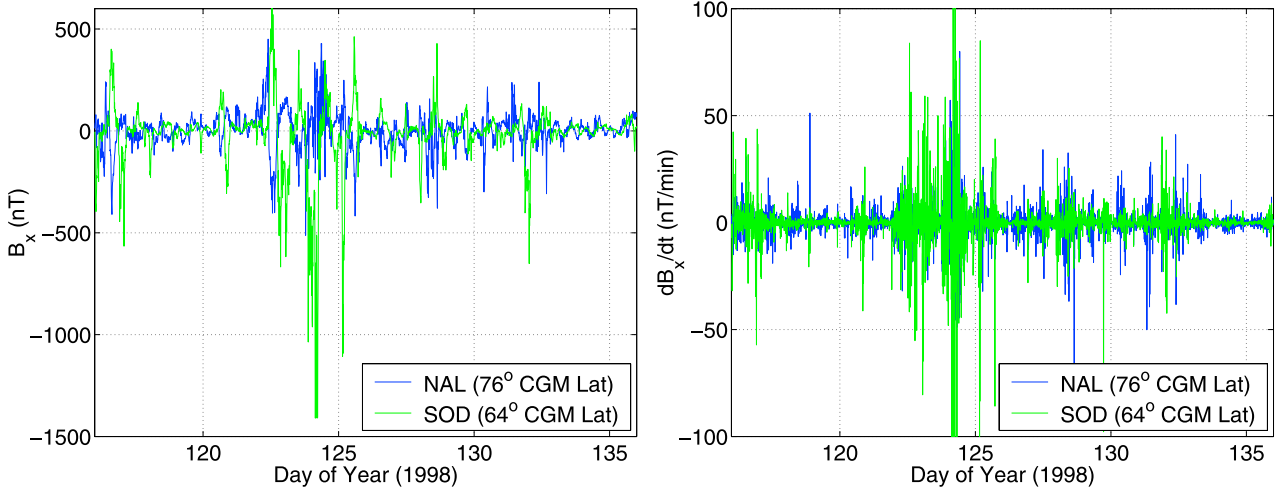


Figure 2. Time series from lower polar-cap station magnetometer station *NAL* (Ny Ålesund) and auroral zone station *SOD* (Sodankylä). (left) North-south component of the ground magnetic field, B_x , at 1-minute resolution. (right) dB_x/dt .

eter and an auroral zone magnetometer. For B_x the amplitude and the standard deviation are larger in the auroral zone time series. The time rate of change of B_x contains more high-frequency fluctuations and has bursts at times when the amplitude of the field B_x is in general quiet. For example, around day 119 of Figure 2a, B_x is in the range ± 100 nT at *NAL*, while a burst of 50 nT/min appears in $|dB_x/dt|$ at *NAL* on the same day, as shown in Figure 2b. This is one indication that the amplitude and time derivative of the field are not driven by the same process; this conclusion is more clearly established by the *PE* surfaces given in the next section.

[24] Figures 3a–3f show a spatial view of the average values of B_\perp and $|dB_\perp/dt|$ as a function of magnetic local time and latitude. The averages are the values of D_{LT}^n over the 2-year data set. The average value at each magnetometer was subtracted off so that the mean value at any latitude is zero. In Figure 3a the locations of largest $|B_x|$ are in the predusk and postmidnight sectors. These locations correspond to the average positions of the eastward and westward electrojets. The peak at $MLT = 0300$ corresponds to the location where *AL* receives its most frequent contribution [Allen and Kroehl, 1975]. The peak positions in $|dB_x/dt|$ in Figure 3b are roughly at the locations where there is a transition from positive to negative values in the average values of B_x ($MLT = 0900$ and 2300). The dayside peak in the $|dB_x/dt|$ surface is at a higher latitude than the nightside peak. The peaks in $|dB_x/dt|$ are not located at the position where the average of the amplitude of $|B_x|$ is the largest. This indicates that the average value of $|dB_x/dt|$ is not as much influenced by (or correlated with) the background amplitude of the field as it is by the transition that must occur when the direction of the average overhead equivalent current system changes sign. In addition, the nightside peak is near the location as the rapidly developing substorm current system, which causes rapid changes in the local field.

4. Average Levels of Coupling

[25] Having evaluated some of the properties of the average disturbance levels, we can now consider the spatial

dependence of the predictability of these quantities by a generalized nonlinear coupling model. The first case considered uses only $\mathbf{I} = [v_x, B_z^{\text{IMF}}]$; the role of the ion density and B_y^{IMF} are considered in a later section.

[26] Given the setup of the model described in section 2, the interpretation of the prediction efficiency, *PE*, is of both a measure of coupling and predictability. When the prediction efficiency is high, the fluctuations are predictable and the measurements are said to be highly coupled to the solar wind. If the prediction efficiency is low, then either the system is not highly coupled or the coupling is not detectable. The coupling may not be detectable for many reasons. The most common reason is that internal magnetospheric fluctuations, not driven or derivable from the available solar wind data, tend to dominate the signal.

[27] We are using the word “prediction” in the sense that only data from time prior to the prediction time is used. Thus we have not smoothed or filtered the input or output signals using data from after the prediction time (a noncausal filtering). Such noncausal smoothing will artificially increase the prediction efficiency because the smoothed data will contain information from after the prediction time. Examples of noncausal prefiltering include using only the time series from the first several components of a singular value decomposition or using the time series generated by removing the high-frequency Fourier components of the original data. Furthermore, a causal prefiltering (e.g., a moving average filter) of the input data was not performed because the mapping function f can act as its own causal prefilter.

[28] Recall that each 30 min in local time and each magnetometer has a different mapping function determined directly from the in-sample data. The spatial results presented in the following figures were obtained by (two-dimensional) 2-D linear interpolation of the out-of-sample *PE* of the mapping functions at 576 points ($= 48(\text{local times}) \times 12(\text{magnetometers})$).

[29] In Figure 4a the level of coupling of B_x to the solar wind is shown in terms of the *PE* of the model on out-of-sample data. In the range of $MLT = [2200, 1000]$ and $[1200, 2000]$ the prediction performance of the model is largest.

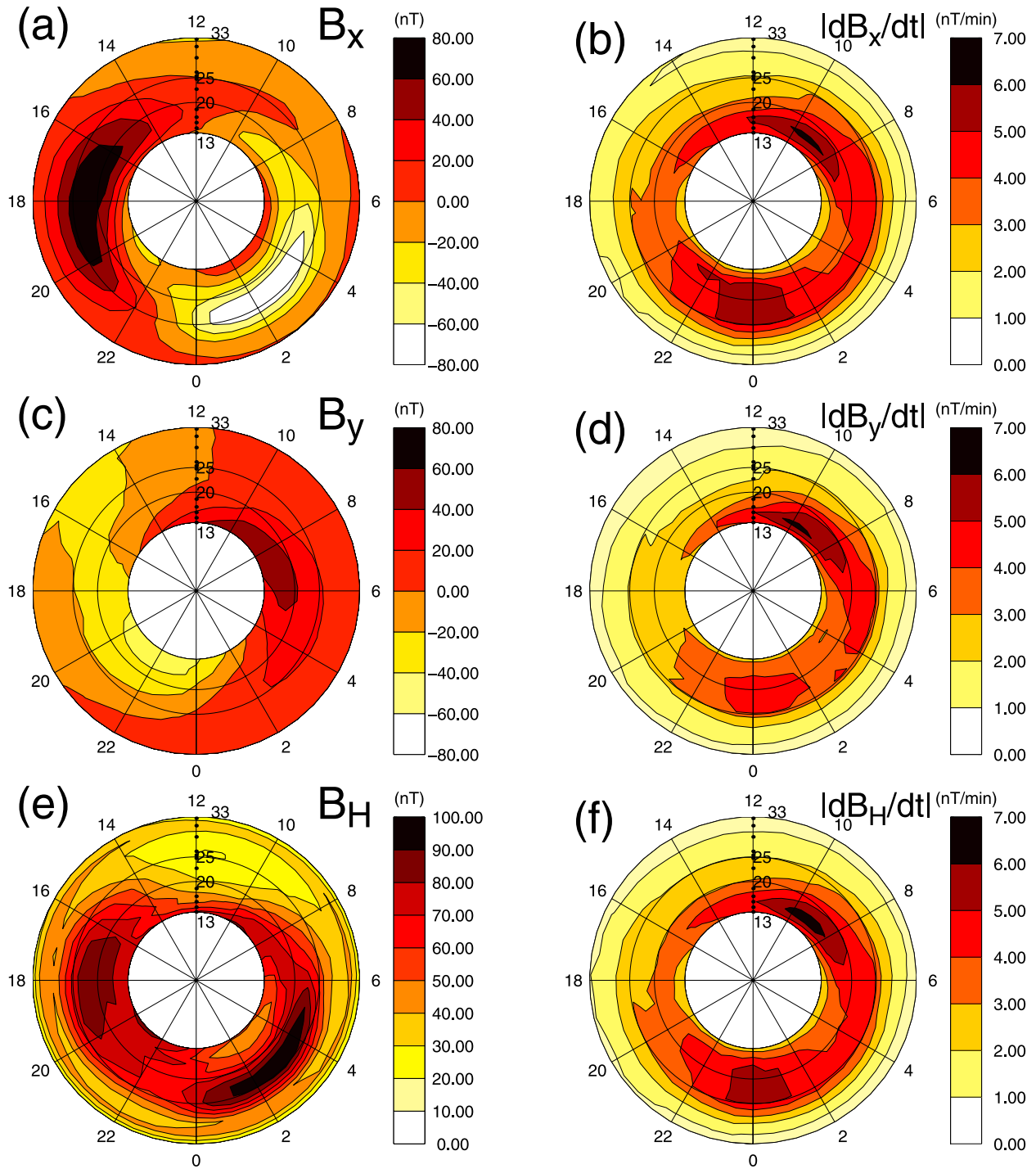


Figure 3. Averages of disturbance measures as a function of CGM MLT and CGM latitude for (a) B_x , (b) $|dB_x/dt|$, (c) B_y , (d) $|dBy/dt|$, (e) B_H , and (f) $|dB_H/dt|$. The dots on the noon axis indicate the CGM latitude of the magnetometers listed in Table 1. The overall average value at each latitude was removed so that the mean at a given latitude is zero.

These surfaces correspond to the expanded auroral oval current systems. We conclude that the elevated PE values are a result of current enhancements that occur during disturbed times for the following reasons. The equivalent ionospheric currents are highly elevated in these regions during times when the IMF is southward for greater than approximately 20 min. The elevated PE is due to this

location being sensitive to changes in the IMF and to the fact that the average current systems occur at a similar location. This claim is reinforced in the following section where the model is shown to be capturing the reconnection driving of auroral-zone current systems.

[30] It is important to recognize that different components of the ground magnetic field will have different PE s. In this

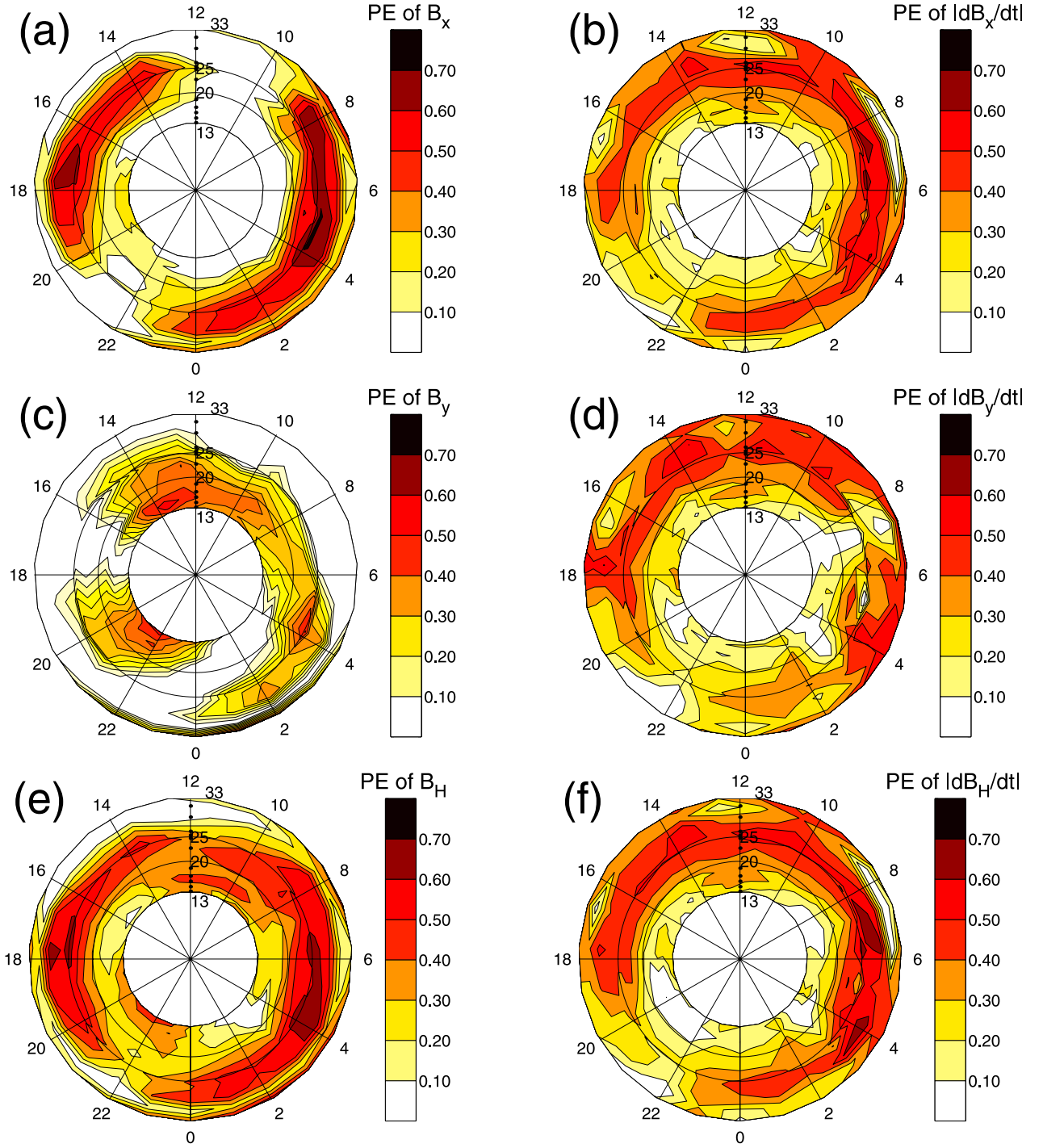


Figure 4. Average PE of disturbance models given solar wind input $\mathbf{I} = [v_x, B_z^{\text{IMF}}]$ that specify (a) B_x , (b) $|dB_x/dt|$, (c) B_y , (d) $|dB_y/dt|$, (e) B_H , and (f) $|dB_H/dt|$.

work, the x (north-south) direction was considered first because of its connection with eastward and westward flowing ionospheric currents in the auroral zone. (For the magnetometers listed in Table 1 the maximum angle between geographic and geomagnetic north is 12 degrees.) The PE is expected to be dependent on direction because of the effect of the geometry of the current systems on the PE . In the locations where the average amplitude of $|B_x|$ has peaks, as shown in Figure 3a, the geographic x -coordinate

system is nearly perpendicular to the equivalent current system DP2 [Clauer and Kamide, 1985; Kamide and Baumjohann, 1993]. This points to the reason that the PE is small near MLT = 1100 and 2100. At these locations there is a transition from east-west current systems to north-south directed currents. At these local times the PE of B_y is large, as shown in Figure 3c, because the dominant direction of the current system has rotated by 90 degrees. In addition, $PE(B_y)$ is comparable to $PE(B_x)$ in the postmidnight sector,

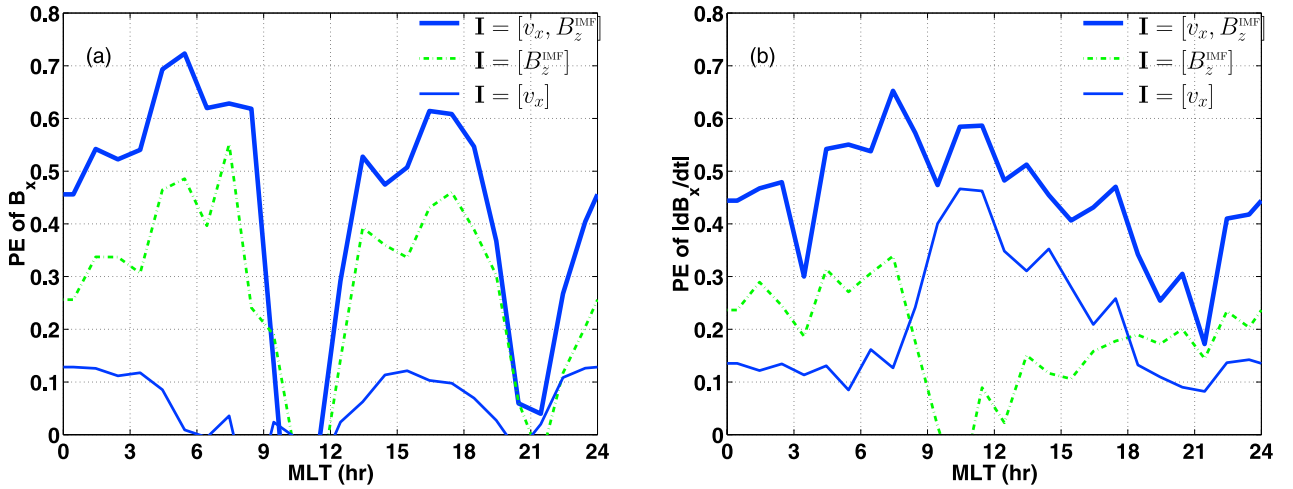


Figure 5. Relative contributions to the PE curve at auroral zone station SOD for (a) the PE of B_x and (b) the PE of $|dB_x/dt|$.

indicating that the model is capturing north-south flowing as well as east-west flowing (equivalent) currents.

[31] In Figure 4e the PE of the horizontal component, $B_H = (B_x^2 + B_y^2)^{1/2}$, is shown. In general the PE s are not always expected to be additive, (e.g., $PE(B_H) \neq PE(B_x) + PE(B_y)$). For example, if $PE(B_y)$ is small and the amplitude of B_y is much larger than that of B_x , then $PE(B_H)$ will be more nearly equal to $PE(B_y)$. Comparison of Figures 4c and 4e shows that generally $PE(H) = PE(B_x) + PE(B_y)$ if either $PE(B_x)$ or $PE(B_y)$ is zero, however.

[32] In Figure 4b the level of coupling of $|dB_x/dt|$ to the solar wind, in terms of the PE of the model, is shown. In general, the PE is highest in the auroral zone and has a slight minimum in the premidnight sector. This figure is a reproduction of the work of Weigel *et al.* [2002]. The PE surface is much less ordered than that of B_x and extends to a higher and lower latitudes. In Figures 4d and 4f the PE surfaces are similar to that of $|dB_x/dt|$. The model for the time rate of change does not capture the dynamics of any one direction better than the others. This is due to the fact that the model is capturing driving by several different processes and is in part driven by a process that does not have a strong directional preference, as discussed in the following section.

5. Relative Contribution of Solar Wind Inputs by Spatial Location

[33] In this section we determine the information content of different solar wind plasma and field measurements. A separation of the measurements is made because different components can drive different processes, and an exact coupling function is not always known. One advantage of using the data-derived approach, in which the optimal coupling function is determined without assuming a form of the coupling function or its inputs, is that the contribution to the PE of each variable can be determined independently. In this section two solar wind variables are considered: v_x and B_z^{IMF} ; the role of the ion density and B_y^{IMF} are considered in the next section.

[34] To compute the relative contribution of a variable to the PE , a reduced model is constructed using only that

variable as an input in equation (3). The influence of this variable is then determined by comparing the PE of the reduced model with one which uses all of the variables in \mathbf{I} . Because the PE is dominated by contributions from v_x and B_z^{IMF} , we begin with these two variables.

[35] In Figure 5a the local time profile of $PE(B_x)$ for the auroral-zone magnetometer station SOD is shown. As expected from studies that couple AL to $v_x B_s$, both the solar wind velocity and magnetic field individually have a nonzero PE . The PE amplitude in the postmidnight sector of approximately 0.6 is also consistent with these studies [Bargatze *et al.*, 1985; Baker, 1986, and references therein]. The PE curve for both v_x and B_z^{IMF} have a similar local time profile. This is expected for a coupling function that is the product of these two variables, i.e., the rectified cross-tail electric field $v_x B_s^{IMF}$. The local time profile for the overall PE curve is similar to that found by Gleisner and Lundstedt [2001], who used a different mapping procedure for the same magnetometer station in the time range of 1978–1985.

[36] The PE of $|dB_x/dt|$ is shown in Figure 5b. The $PE(\mathbf{I} = [v_x])$ curve is higher than the $PE(\mathbf{I} = [B_z^{IMF}])$ curve in the prenoon sector. This implies that v_x is the most important driver of $|dB_x/dt|$, while the solar wind magnetic field B_z^{IMF} has a comparatively smaller contribution. The optimal coupling function is highly dependent on LT . For example, at $LT = 1100$ the mapping function does not depend on B_z^{IMF} . This result reveals the importance of allowing for a data-derived coupling function. If a form such as $I = v_x B_s^{IMF}$ was used, the PE curve would be zero in the locations where the $PE(\mathbf{I} = [B_z^{IMF}])$ curve of $|dB_x/dt|$ is zero because the B_z^{IMF} signal randomizes the correlation of $|dB_x/dt|$ with v_x .

[37] The interpretation of the v_x profile in Figure 5b follows from the solar wind driving of ULF disturbances. Vennerström [1999] has shown that the power spectral density (PSD) of H in the 2–10 min band is enhanced from the prenoon sector to the midnight sector, with peaks at $MLT = 0800$ and 2300 . The local time profile of the PE in Figure 5b follows the local time profile of the amplitude of the PSD of these ULF fluctuations. Because they are correlated, $|dB_x/dt|$ is an indirect measure of $PSD(H)$; locations with a high amplitude of $PSD(H)$ will have a high

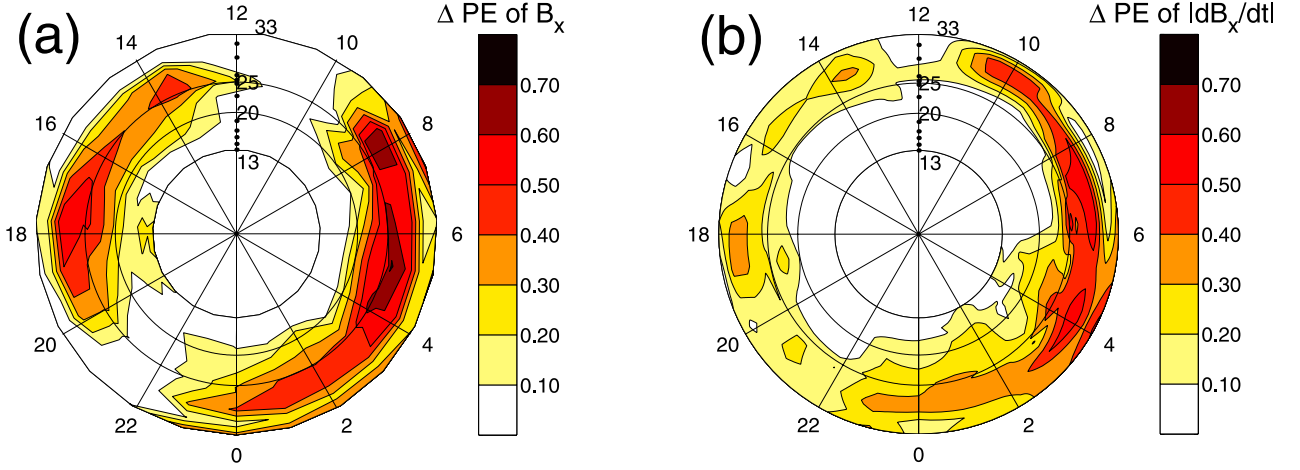


Figure 6. PE difference between a model that uses $\mathbf{I} = [v_x, B_z^{\text{IMF}}]$ and one that uses only $\mathbf{I} = [v_x]$ as an input to specify (a) B_x and (b) $|dB_x/dt|$. In locations with large ΔPE , B_z^{IMF} is a primary driver of activity.

average value of $|dB_x/dt|$. The PE value of 0.55 at MLT = 0600 is consistent with the in-sample correlation $R^2 = 0.5$ between v_x and $PSD(H)$ found by Vennerström [1999]. The driving of dayside ULF waves by v_x can be explained by the Kelvin-Helmholtz instability [Southwood, 1968]. The asymmetry of the distribution about noon has been shown by Lee and Olson [1980] to be due to typical IMF configurations which make the instability more likely to occur on field lines that map to the prenoon sector.

[38] In Figures 6 and 7 a global view of the above observations is shown. The procedure for testing the influence or importance of an input variable is the same: two models are compared, one that uses a variable as an input and one that does not. The surfaces in Figure 6 are computed from the difference

$$\Delta PE = PE(\mathbf{I} = [v_x, B_z^{\text{IMF}}]) - PE(\mathbf{I} = [v_x]). \quad (10)$$

If ΔPE is positive, then a model that uses B_z^{IMF} is superior to a model that does not. If ΔPE is small, then B_z^{IMF} has a small influence, provided that $PE(\mathbf{I} = [v_x, B_z^{\text{IMF}}])$ is not also

small; this can be checked in Figure 4. Ideally, a plot of the relative improvement, $\Delta PE/PE(\mathbf{I} = [v_x])$, would be made, but this is not done because $PE(\mathbf{I} = [v_x])$ can be zero.

[39] Figure 6a shows that the independent contribution of B_z^{IMF} to $PE(B_x)$ is the largest in the location of the eastward and westward electrojets in the expanded auroral oval. Because the model primarily captures the reconnection driving of these systems, the surface of the independent contribution of v_x shown in Figure 7a has similar features.

[40] In Figure 6b the independent contribution of B_z^{IMF} to $PE(|dB_x/dt|)$ is primarily in the postmidnight sector. The midnight sector enhancements are due to the influence of B_z^{IMF} in driving both electrojet and substorm-like fluctuations, both of which drive dB_x/dt . Figure 7b shows that as expected from the driving of ULF activity by v_x , the independent contribution of v_x to $PE(|dB_x/dt|)$ is elevated in the prenoon sector.

6. Role of B_y^{IMF} and ρ_i

[41] In the previous section, only the relative contribution of v_x and B_z^{IMF} to model performance was considered.

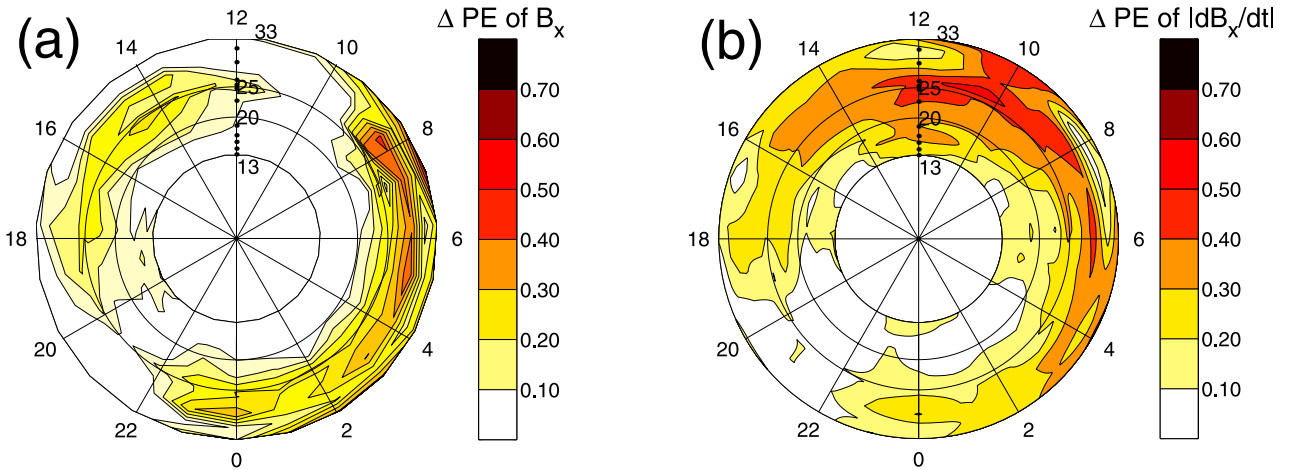


Figure 7. PE difference between a model that uses $\mathbf{I} = [v_x, B_z^{\text{IMF}}]$ and one that uses only $\mathbf{I} = [B_z^{\text{IMF}}]$ as an input to specify (a) B_x and (b) $|dB_x/dt|$. In locations with large ΔPE , v_x is a primary driver of activity.

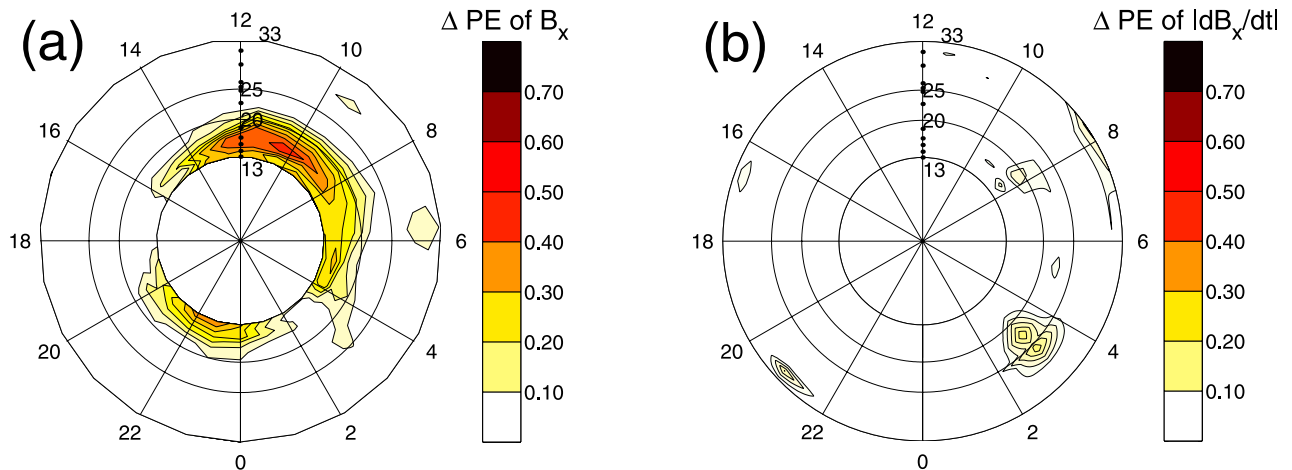


Figure 8. PE difference between a model that uses $\mathbf{I} = [v_x, B_z^{\text{IMF}}, B_y^{\text{IMF}}]$ and one that uses only $\mathbf{I} = [v_x, B_z^{\text{IMF}}]$ as an input. In locations with large ΔPE , B_y^{IMF} is a primary driver of activity. (a) Model that specifies B_x . (b) Model that specifies $|dB_x/dt|$.

Various studies of high-latitude geomagnetic indices such as AE have shown that both B_y^{IMF} and ρ_i only slightly improve the data-model correlation. For example, *Gleisner and Lundstedt* [1997] have shown a neural network model that predicts AE given $\mathbf{I} = [v_x, B_z^{\text{IMF}}, \rho_i]$ has $R^2 = 0.73$, while a model that uses $\mathbf{I} = [v_x, B_z^{\text{IMF}}]$ yields $R^2 = 0.69$, corresponding to $\Delta PE \simeq 0.04$. Thus B_y^{IMF} and ρ_i independently account for very little of the variance of the AE index.

[42] In contrast, the average amplitude of PC and $AL/(B_s + 0.5)v^2$ has been shown to have a strong dependence on B_y^{IMF} [Vennerström and Friis-Christensen, 1987; Aoki, 1977; Murayama et al., 1980]. Moreover, the epoch average of the PC index has a dependence on B_y^{IMF} [Troshichev et al., 1986]; a recent event study [Shue and Kamide, 2001] showed an example of a ground magnetic field response that coincided with an increase in the solar wind density while the velocity and IMF were steady.

[43] These results are not necessarily contradictory. It is possible that a variable has a physical significance but does not improve the prediction of the dynamics when included as a model input. A variable with physical significance may not improve model performance for many reasons, but most often either the variable generates a process that does not occur frequently, its physical role cannot be distinguished from a different variable because the two variables are highly correlated, or the relative noise level is high. Also, the process used to generate the mapping function may obscure the influence of a driving variable if the driver's influence is seasonally dependent. In the present analysis the method used to generate the mapping function used data from all seasons. Thus the influence of a variable which has a true mapping function that reverses sign with season will be suppressed. A seasonal reversal in the mapping function that relates B_y^{IMF} to the disturbance quantity $AL/(B_s + 0.5)v^2$ was found by *Murayama et al.* [1980]. Also, a seasonal dependence in the mapping function that relates B_y^{IMF} to the polar-cap index, PC , was found by *Vennerström and Friis-Christensen* [1987].

[44] Conventionally, the word “driver” is used for a variable that independently improves the model PE when it is included as a model input. However, a variable that

does not improve the model PE can also be a driver on different time or space scales. For this reason, we restrict our meaning of nondriver to mean a variable that does not independently explain any of the PE with respect to the experiment, i.e., the time scale, spatial scale, and data range under consideration.

[45] The independent influence of B_y^{IMF} on the PE is tested by comparing two models that are derived using the same magnetometer data, one which uses $\mathbf{I} = [v_x, B_z^{\text{IMF}}, B_y^{\text{IMF}}]$ and the other which uses only $\mathbf{I} = [v_x, B_z^{\text{IMF}}]$ as the input. The process for testing the influence of ρ_i is the same.

[46] In Figure 8a the difference, $\Delta PE(B_x)$, between a model that uses B_y^{IMF} versus one that does not is shown. The improvement in $PE(B_x)$ is less than 0.10 in auroral zone locations. This result shows that a model which specifies the 30-min average of B_x , given six previous 30-min averages of $\mathbf{I} = [v_x, B_z^{\text{IMF}}, B_y^{\text{IMF}}]$, has a PE that is less than 0.10 larger than a model that uses only $\mathbf{I} = [v_x, B_z^{\text{IMF}}]$ at all auroral zone latitudes. This is consistent with *Gleisner and Lundstedt* [1997] and *Baker* [1986] who found that the difference in data-model correlation was less than 0.10 when the modeled data was AE or AL .

[47] The most robust feature of Figures 8a and 9a is the improvement at the highest latitudes. This is an indication that the driver of the processes that the model is capturing has a dependence on both B_y^{IMF} and ρ_i .

[48] At auroral-zone latitudes the contribution of the variables B_y^{IMF} and ρ_i to the coupling is substantially lower than what is expected from theoretical energy transfer rates. For example, the reconnection relation [Gonzalez and Gonzalez, 1984] $v_x(B_y^{\text{IMF}2} + B_z^{\text{IMF}2})^{1/2} \sin^2(\theta/2)$ overestimates the influence of B_y^{IMF} , as noted by *Vennerström and Friis-Christensen* [1987]. That result is bolstered by the finding that the overall error is only marginally improved if B_y^{IMF} is included in a geomagnetic index prediction filter [Gleisner and Lundstedt, 1997]. One possible reason for this lies in the assumption that on the time scale considered, the energy deposited on the ionosphere, as measured by a geomagnetic index or the ground magnetic field, is proportional to the energy transfer function that applies at the magnetosphere boundary. Much of the energy circulates through the magne-

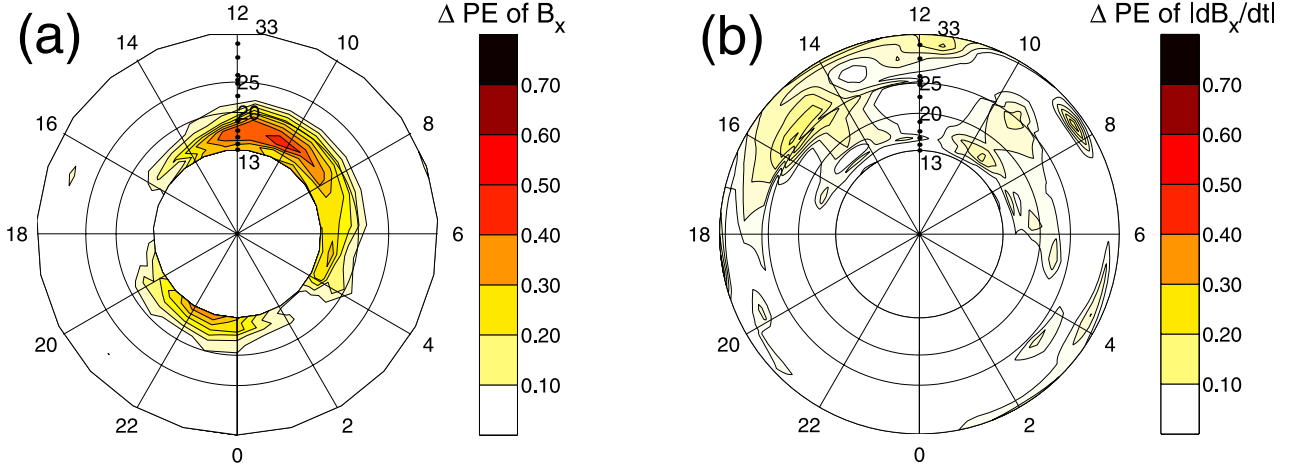


Figure 9. PE difference between a model that uses $\mathbf{I} = [v_x, B_z^{\text{IMF}}, \rho_i]$ and one that uses only $\mathbf{I} = [v_x, B_z^{\text{IMF}}]$ as an input. In location with large ΔPE , ρ_i is a primary driver of activity. (a) Model that specifies B_x . (b) Model that specifies $|dB_x/dt|$.

tosphere and flows through many other regions before it is deposited on the ionosphere. Therefore it is expected that the mapping function dependence on B_y^{IMF} and ρ_i that applies at the ground is not the same as what applies at the magnetosphere boundary. This is especially expected in locations where the connection to the energy source is highly indirect, for example, at lower auroral-zone latitudes.

[49] Figures 8b and 9b show that B_y^{IMF} and ρ_i have a small influence on $|dB_x/dt|$ in most locations considered. There is a slight response to ρ_i in the postnoon sector. This may be due to a pressure pulse influence; a future work will consider this hypothesis in more detail.

7. Mapping Function

[50] To evaluate the level of nonlinearity in the coupling function, the PE from the nonlinear mapping function of equation (9) is compared with its linearized version (i.e., a linear moving average filter). That is, the model of equation (9) is compared with

$$f_{LT}^m(\mathbf{X}) = \sum_{i=1}^N w_i^{m,LT} X_i + w_o^{m,LT}, \quad (11)$$

where $LT = [0.0, 0.5, 1.0, \dots, 23.5]$ and the 30-min averaged propagation-delayed solar wind data is, as before,

$$\mathbf{X}(t) = [\mathbf{I}(t - t_d), \mathbf{I}(t - t_d - t_a), \mathbf{I}(t - t_d - 2t_a), \dots, \mathbf{I}(t - t_d - 5t_a)] \quad (12)$$

$$\mathbf{I}(t) = [\rho_i(t), B_y^{\text{IMF}}(t), B_z^{\text{IMF}}(t), v_x(t)]. \quad (13)$$

This linear formulation is similar to the IZMEM model [Papitashvili et al., 1994], which uses $LT = [0, 1, \dots, 23]$ and 1-hour averages of the solar wind variables

$$\mathbf{X}(t) = [B_x^{\text{IMF}}(t), B_y^{\text{IMF}}(t), B_z^{\text{IMF}}(t), v^2(t), \rho_i(t)v^2(t)], \quad (14)$$

which are not propagation-delayed. This equation is pre-nonlinearized in the sense that the form of the nonlinearity in v_x is specified.

[51] Figures 10a and 10b show $\Delta PE = PE_{\text{nonlinear}} - PE_{\text{linear}}$ for the B_x and $|dB_x/dt|$ models. If ΔPE is positive, then a nonlinear model is superior to a linear model. If ΔPE is small, then, with respect to the data set and numerical setup, a nonlinear mapping function performs no better than a linear one (provided that $PE_{\text{nonlinear}}$ is not also small; this can be checked in Figure 4).

[52] For both B_x and $|dB_x/dt|$, the nonlinearity is centered in the lower auroral zone latitudes. This is consistent with studies of the coupling between the solar wind and AL which find that the most simple form of a nonlinear coupling function is $v_x B_s^{\text{IMF}}$, where B_s^{IMF} is the southward component of the IMF. Clearly, in these locations, the rectification (a nonlinear operation) of B_z^{IMF} is important; this reinforces the conclusion that the disturbances are strongly driven by the reconnection process. At other locations, a linear model is as good as a model that has possible solutions that are an arbitrary functional form of the solar wind variables. These surfaces also show how a coupling function should be structured to save computational time because they reveal locations where increased attention to nonlinearities in empirical models should yield the most improvement.

[53] Most of the nonlinearity in the model is with respect to B_z^{IMF} . In Figure 11 the mapping function for the nonlinear model is shown at different values of B_z^{IMF} , holding all other inputs fixed at their average values. Figure 11a shows this mapping function at different local times for $D = B_x = f(\mathbf{I} = [B_z^{\text{IMF}}, \bar{v}_x])$ at auroral zone magnetometer SOD . At noon, where the nonlinear model was only slightly better than the linear model (from Figure 11a), the mapping curve is nearly flat. At the two nightside local times there is substantial curvature in the mapping function, and the reduction in output (rectification) of positive B_z^{IMF} is clearly seen. Figure 11b shows these same curves for the $D = |dB_x/dt| = f(\mathbf{I} = [B_z^{\text{IMF}}, \bar{v}_x])$ mappings. Here, the nonlinear model has the same PE as the linear model at noon, and for this reason the $LT = 1200$ curve is nearly a straight line. The two nightside

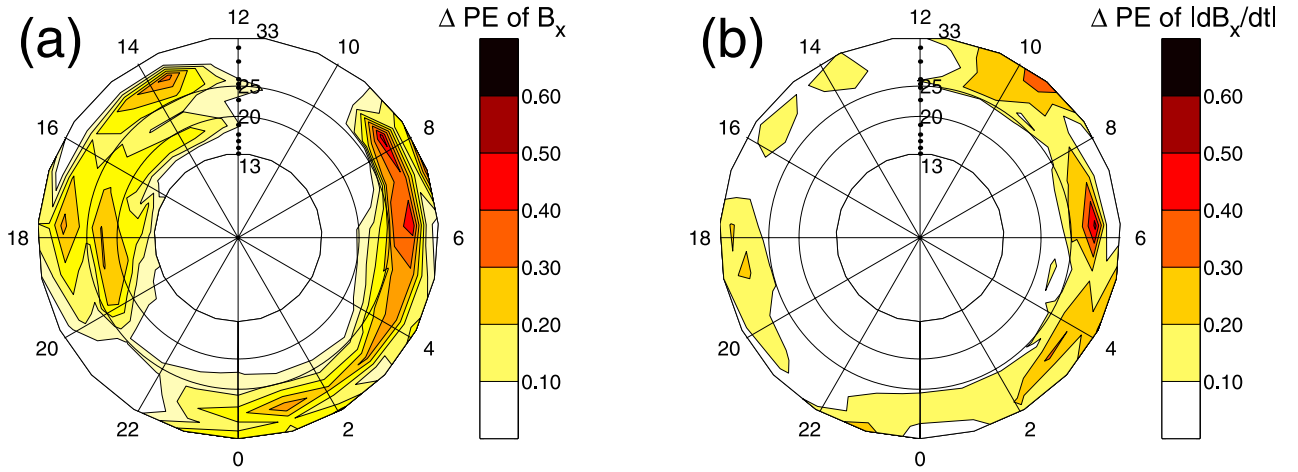


Figure 10. Spatial distribution of the nonlinearity in the solar wind coupling function that specifies (a) B_x and (b) $|dB_x/dt|$. Locations with high ΔPE occur where the nonlinear model is better than the linear model. Locations with small ΔPE and nonzero $PE_{\text{nonlinear}}$ (in Figure 4) are the positions where the linear model performs as well as the nonlinear model.

locations have both curvature and a reduction in output for positive values of B_z^{IMF} .

8. Discussion and Conclusions

[54] This paper presented the prediction error and prediction properties of a generalized data-derived nonlinear mapping function that specifies the ground magnetic field and its time derivative given the solar wind state. From these data-derived coupling functions the following questions were answered for 30 min time scales:

[55] 1. How closely can we expect to model ground magnetic fields and their time derivatives at a high-latitude location given only measurements from a single location in the upstream solar wind (i.e., the expected prediction error or data-model correlation)?

[56] To answer these questions for a general class of high-latitude models that are driven by solar wind measurements, a general nonlinear statistical filter, in the form of a

neural network, was used. For B_x , the highest data-model correlation is in the postmidnight and postnoon sectors at auroral zone latitudes. In the prenoon and premidnight sector the data-model correlation is small. The PE of different components of the ground magnetic field was also considered. At auroral zone latitudes, the north-south component, B_x , has the highest PE due to its perpendicular alignment with the DP equivalent current system. At higher latitudes the east-west component B_y contains a PE that is comparable to that of B_x . The total horizontal field, B_H has a PE that does not contain the dropouts that are evident in $PE(B_x)$.

[57] For $|dB_x/dt|$, the data-model correlation is elevated throughout the auroral zone and the high- PE surface extends to much lower latitudes. For $|dB_y/dt|$, the PE is large at auroral zone amplitudes and is comparable to $PE(|dB_x/dt|)$.

[58] The conventional view is that the nightside auroral zone should be less predictable than other locations because

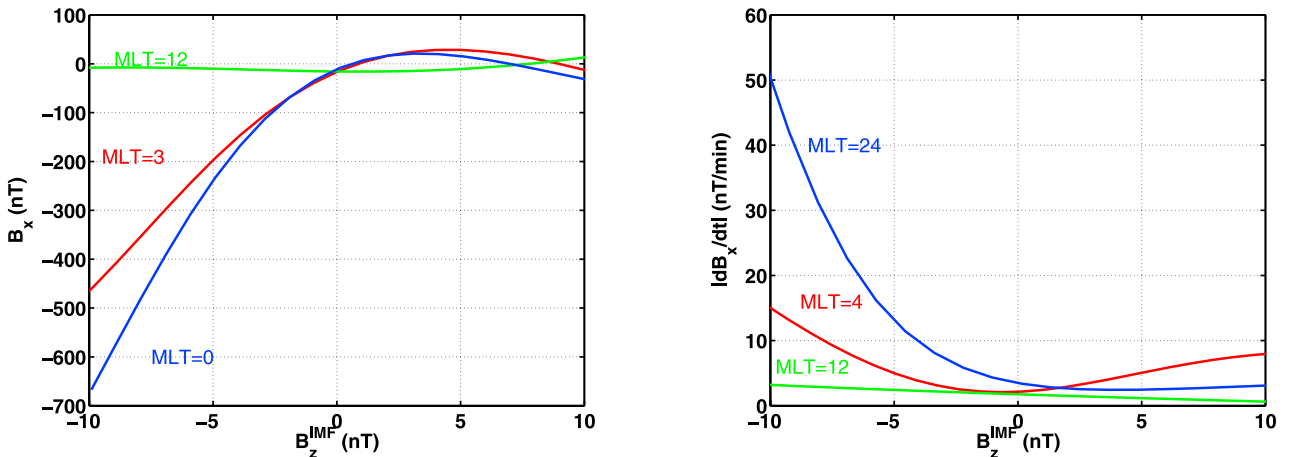


Figure 11. Relationship between B_z^{IMF} and the output disturbance level at SOD for (left) $D = B_x$ and (right) $D = |dB_x/dt|$.

of substorm activity. Figure 4 shows that this is not the case. The PE is higher in the auroral zone because it is the most active and sensitive to changes in the solar wind; it has more dynamic behavior that can be captured. There is still an unpredictable component, however, because approximately 40% of the variance is not captured. However, the substorm effect in lowering the PE is less than the effect of the other factors that caused low PE s in the prenoon and premidnight sectors.

[59] 2. Which solar wind variables give the most information about the state of the ground magnetic field at a given location?

[60] This question was a primary motivation for developing a model that allows the solar wind inputs to be included separately, as opposed to the use of a prescribed or predetermined energy coupling function. By determining the optimal coupling function from the data, we have shown that no single solar wind input coupling function (i.e., $v_x B_s$, $v_x^2 B_s$, etc.) is appropriate for all spatial locations. By separately considering each variable and computing how much influence it has on explaining the data, it was shown that the process that drives B_x is different from that which drives $|dB_x/dt|$. For B_x , the north-south component of the ground magnetic field, v_x and B_z^{IMF} are the most important drivers when used as model inputs; they explain most of the variance of the B_x time series at auroral zone latitudes. The data-derived approach was especially useful for $|dB_x/dt|$ because a theoretical coupling function has not been developed. For $|dB_x/dt|$, the form of the coupling is sensitive to local time. At 1000 MLT, v_x has the greatest influence and B_z^{IMF} has nearly no influence on the PE ; however, in the postmidnight sector B_z^{IMF} explains a substantial portion of the $|dB_x/dt|$ variance while v_x has a much smaller role.

[61] This analysis can be used to test the relative importance of reconnection driving and Kelvin-Helmholtz driving of $|dB_x/dt|$. In locations where the PE is dependent only on v_x , reconnection can be ruled out as a driver. Locations where the PE has a dependence on both v_x and B_z^{IMF} reveal a strong reconnection influence.

[62] The influence of ρ_i and B_y^{IMF} was tested by computing the change in PE when they were added as an input to the model. In this analysis both variables were found to be weak drivers of activity at auroral zone latitudes because they provided only a marginal increase in the data-model correlation (PE) of B_x and $|dB_x/dt|$. The conclusions drawn here with regard to ρ_i are similar to O'Brien and McPherron [2000] who conclude that ρ_i does not drive D_{st} , using linear correlation analysis of a large set of magnetic storms on a time scale of a few hours.

[63] The method used for computing the mapping function may obscure the influence of a driving variable if the driver's influence is seasonally dependent. The average PE was computed by generating 20 models using a random sample of training and test set data from all seasons. This method may obscure the influence of a driving variable if the driver's influence is seasonally dependent. Seasonal dependencies in the mapping function that relates B_y^{IMF} to polar-cap disturbances have been found by Vennerström and Friis-Christensen [1987]. At auroral zone latitudes, Murayama et al. [1980] showed the mapping function that relates B_y^{IMF} to the disturbance quantity $AL/(B_s + 0.5)v^2$ reversed sign with season.

[64] Preliminary tests with the 2-year data set have shown that a PE dependence on season may also exist. However, the PE depends on the average amplitude of the disturbance measure being predicted, which also has a seasonal dependence. Therefore to isolate the dependence of PE on season with statistical significance, a analysis of data set that covers more than 2 years is needed.

[65] The data-derived approach is in contrast to models of the mapping of solar wind measurements onto geomagnetic quantities in which the coupling function is assumed to be proportional to a energy transfer rate. These models generally assume that the energy transfer rate at the magnetospheric boundary (reconnection location) is proportional to a geomagnetic index. Although appealing because they use equations based on a physical energy transfer mechanism, these methods often produce results in which complex combinations of many variables (e.g., $[\rho_i, B_y^{\text{IMF}}, B_z^{\text{IMF}}, v_x]$) produce nearly the same data-model correlation as very simplified forms of fewer variables (e.g., $[v_x, B_z^{\text{IMF}}]$) [Baker, 1986; Wu and Lundstedt, 1997; Gleisner and Lundstedt, 1997]. In addition, the theoretical forms of the energy transfer equation often overestimate the contribution of $[\rho_i, B_y^{\text{IMF}}]$, as noted by Vennerström and Friis-Christensen [1987]. A probable reason for this is that the mapping of energy quantities from the magnetospheric boundary to ionospheric disturbance measures is not linear. This is especially true on time scales of less than several hours because much of the energy introduced via reconnection has not been dissipated [Vasyliunas et al., 1982].

[66] 3. How does the form of the optimal coupling function change as a function of spatial location?

[67] There are three ways to answer this. First, locations where the influence of a variable on the PE is zero show where this variable should not be in a parsimonious coupling function. For example, in the case of $|dB_x/dt|$, B_z^{IMF} had nearly no influence on the PE in the prenoon sector. Second, by comparing the PE s of a linear model with that of a nonlinear model, locations where a parsimonious coupling function is linear are revealed. For B_x and B_H , most of the nonlinearity is found at auroral zone latitudes. For the time derivatives the nonlinearity was primarily in the nightside auroral zone sector. Finally, by plotting the data-derived coupling function according to MLT and latitude, changes in its form can be detected. From this, it was shown that the nonlinearity was primarily due to the rectification of B_z^{IMF} , and its sensitivity to B_z^{IMF} depended on spatial location.

[68] **Acknowledgments.** We thank the institutes that maintain the IMAGE magnetometer array: the PI institute for IMAGE, the Finnish Meteorological Institute (www.geo.fni.fi/image), and the Space Radiation Laboratory at Caltech which provided the online ACE solar wind data.

[69] Arthur Richmond thanks Susanne Vennerström and Ari Viljanen for their assistance in evaluating this paper.

References

- Akasofu, S. I., Inter-planetary energy flux associated with magnetospheric substorms, *Planet Space Sci.*, 27, 425–431, 1979.
- Allen, J., and H. Kroehl, Spatial and temporal distributions of magnetic effects of auroral electrojets as derived from ae-indices, *J. Geophys. Res.*, 80, 3667–3677, 1975.
- Aoki, T., Influence of dipole tilt angle on development of auroral electrojets, *J. Geomagn. Geoelectr.*, 29, 441–453, 1977.
- Baker, D., Statistical analyses in the study of solar wind-magnetosphere coupling, in *Solar Wind-Magnetosphere Coupling*, edited by Y. Kamide, and J. Slavin, pp. 17–38, Kluwer Acad., Norwell, Mass., 1986.

- Bargatze, L. F., D. N. Baker, R. L. McPherron, and E. W. Hones, Magnetospheric impulse-response for many levels of geomagnetic activity, *J. Geophys. Res.*, **90**, 6387–6394, 1985.
- Bishop, C., *Neural Networks for Pattern Recognition*, Oxford Univ. Press, New York, 1995.
- Boteler, D., R. Pirjola, and L. Trichtchenko, On calculating the electric and magnetic fields produced in technological systems at the earth's surface by a "wide" electrojet, *J. Atmos. Sol. Terr. Phys.*, **62**, 1311–1315, 2000.
- Box, G., and G. Jenkins, *Time Series Analysis: Forecasting and Control*, Holden-Day, Boca Raton, Fla., 1976.
- Clauer, C. R., and Y. Kamide, Dp-1 and dp-2 current systems for the March 22, 1979 substorms, *J. Geophys. Res.*, **90**, 1343–1354, 1985.
- Clauer, C. R., R. L. McPherron, C. Searls, and M. G. Kivelson, Solar wind control of auroral-zone geomagnetic-activity, *Geophys. Res. Lett.*, **8**, 915–918, 1981.
- Cybenko, G., Approximation by superpositions of sigmoidal function, *Math. Control Signals Syst.*, **2**, 303–314, 1989.
- Detman, T., and D. Vassiliadis, Review of techniques for magnetic storm forecasting, in *Magnetic Storms*, *Geophys. Monogr. Ser.*, vol. 98, AGU, Washington, D. C., 1997.
- Fedder, J., S. Slinker, J. Lyon, and R. Elphinstone, Global numerical-simulation of the growth-phase and the expansion onset for a substorm observed by Viking, *J. Geophys. Res.*, **100**, 19,083–19,093, 1995.
- Gavrishchaka, V., and S. Ganguli, Optimization of the neural-network geomagnetic model for forecasting large-amplitude substorm events, *J. Geophys. Res.*, **106**, 6247–6257, 2001.
- Gleisner, H., and H. Lundstedt, Response of the auroral electrojets to the solar wind modeled with neural networks, *J. Geophys. Res.*, **102**, 14,269–14,278, 1997.
- Gleisner, H., and H. Lundstedt, Auroral electrojet predictions with dynamic neural networks, *J. Geophys. Res.*, **106**, 24,541–24,549, 2001.
- Gonzalez, W. D., and A. L. C. Gonzalez, Energy-transfer by magnetopause reconnection and the substorm parameter-epsilon, *Planet Space Sci.*, **32**, 1007–1012, 1984.
- Heppner, J. P., and N. C. Maynard, Empirical high-latitude electric-field models, *J. Geophys. Res.*, **92**, 4467–4489, 1987.
- Horton, W., and I. Doxas, A low-dimension energy-conserving state space model for substorm dynamics, *J. Geophys. Res.*, **101**, 27,223–27,237, 1996.
- Horton, W., and I. Doxas, A low-dimensional dynamical model for the solar wind driven geotail-ionosphere system, *J. Geophys. Res.*, **103**, 4561–4572, 1998.
- Kamide, Y., and W. Baumjohann, *Magnetosphere-Ionosphere Coupling, Physics and Chemistry in Space*, vol. 23, Springer-Verlag, New York, 1993.
- Kelly, T., N. Crooker, G. Siscoe, C. Russell, and E. Smith, On the use of a sunward libration-point-orbiting spacecraft as an interplanetary magnetic-field monitor for magnetospheric studies, *J. Geophys. Res.*, **91**, 5629–5636, 1986.
- Klimas, A. J., D. N. Baker, D. A. Roberts, D. H. Fairfield, and J. Buchner, A nonlinear dynamic analog model of geomagnetic-activity, *J. Geophys. Res.*, **97**, 12,253–12,266, 1992.
- Klimas, A. J., D. N. Baker, D. Vassiliadis, and D. A. Roberts, Substorm recurrence during steady and variable solar wind driving—Evidence for a normal-mode in the unloading dynamics of the magnetosphere, *J. Geophys. Res.*, **99**, 14,855–14,861, 1994.
- Klimas, A., D. Vassiliadis, D. Baker, and D. Roberts, The organized nonlinear dynamics of the magnetosphere, *J. Geophys. Res.*, **101**, 13,089–13,113, 1996.
- Klimas, A. J., D. Vassiliadis, and D. N. Baker, Data-derived analogues of the magnetospheric dynamics, *J. Geophys. Res.*, **102**, 26,993–27,009, 1997.
- Klimas, A., D. Vassiliadis, D. Baker, and J. Valdivia, Data-derived analogues of the solar wind-magnetosphere interaction, *Phys. Chem. Earth, Part C*, **24**, 37–44, 1999.
- Lee, L., and J. Olson, Kelvin-helmholtz instability and the variation of geomagnetic pulsation activity, *Geophys. Res. Lett.*, **7**, 777–780, 1980.
- Luhr, H., A. Aylward, S. Bucher, A. Pajunpaa, K. Panjunpaa, T. Holmboe, and S. Zalewski, Westward moving dynamic substorm features observed with the image magnetometer network and other ground-based instruments, *Ann. Geophys.*, **16**, 425–440, 1998.
- McComas, D., S. Bame, P. Barker, W. Feldman, J. Phillips, P. Riley, and J. Griffiee, Solar wind electron proton alpha monitor (SWEPAM) for the advanced composition explorer, *Space Sci. Rev.*, **86**, 563–612, 1998.
- Murayama, T., T. Aoki, H. Nakai, and K. Hakamada, Empirical-formula to relate the auroral electrojet intensity with inter-planetary parameters, *Planet Space Sci.*, **28**, 803–813, 1980.
- O'Brien, T. P., and R. L. McPherron, Evidence against an independent solar wind density driver of the terrestrial ring current, *Geophys. Res. Lett.*, **27**, 3797–3799, 2000.
- Papitashvili, V., B. Belov, D. Faermark, Y. Feldstein, S. Golyshev, L. Gromova, and A. Levitin, Electric-potential patterns in the northern and southern polar regions parameterized by the interplanetary magnetic-field, *J. Geophys. Res.*, **99**, 13,251–13,262, 1994.
- Papitashvili, V., C. Clauer, T. Killeen, B. Belov, S. Golyshev, and A. Levitin, Linear modeling of ionospheric electrodynamics from the IMF and solar wind data: Application for space weather forecast, *Adv. Space Res.*, **22**, 113–116, 1998.
- Pirjola, R., and A. Viljanen, Complex image method for calculating electric and magnetic fields produced by an auroral electrojet of finite length, *Ann. Geophys.*, **16**, 1434–1444, 1998.
- Richmond, A. D., and Y. Kamide, Mapping electrodynamic features of the high-latitude ionosphere from localized observations—Technique, *J. Geophys. Res.*, **93**, 5741–5759, 1988.
- Ridley, A. J., G. Crowley, and C. Freitas, An empirical model of the ionospheric electric potential, *Geophys. Res. Lett.*, **27**, 3675–3678, 2000.
- Rostoker, G., and F. Pascal, Dependence of the response of the magnetosphere ionosphere current systems on the preconditioning of the auroral oval and on the level of the solar terrestrial interaction, *Can. J. Phys.*, **68**, 74–80, 1990.
- Shue, J. H., and Y. Kamide, Effects of solar wind density on auroral electrojets, *Geophys. Res. Lett.*, **28**, 2181–2184, 2001.
- Smith, C., J. L'Heureux, N. Ness, M. Acuna, L. Burlaga, and J. Scheifele, The ACE magnetic fields experiment, *Space Sci. Rev.*, **86**, 613–632, 1988.
- Southwood, D., Hydromagnetic stability of magnetospheric boundary, *Planet Space Sci.*, **16**, 587, 1968.
- Takalo, J., and J. Timonen, Neural network prediction of AE data, *Geophys. Res. Lett.*, **24**, 2403–2406, 1997.
- Troshichev, O., and M. Gusev, IMF B_x and B_y dependencies of the polar-cap auroral distribution for northward IMF orientation inferred from observations at vostok station, *J. Atmos. Terr. Phys.*, **56**, 237–244, 1994.
- Troshichev, O., and N. Voloshinov, Effects of magnetic activity and interplanetary magnetic-field on the position of radioaurorae in the southern polar-region, *Planet Space Sci.*, **36**, 441–448, 1988.
- Troshichev, O., A. Kotikov, B. Bolotinskaya, and V. Andezen, Influence of the IMF azimuthal component on magnetospheric substorm dynamics, *J. Geomagn. Geoelectr.*, **38**, 1075–1088, 1986.
- Valdivia, J., D. Vassiliadis, A. Klimas, and A. Sharma, Modeling the spatial structure of the high latitude magnetic perturbations and the related current systems, *Phys. Plasmas*, **6**, 4185–4194, 1999.
- Vassiliadis, D., A. Klimas, D. Baker, and D. Roberts, A description of the solar wind magnetosphere coupling based on nonlinear filters, *J. Geophys. Res.*, **100**, 3495–3512, 1995.
- Vasyliunas, V. M., J. R. Kan, G. L. Siscoe, and S. I. Akasofu, Scaling relations governing magnetospheric energy-transfer, *Planet Space Sci.*, **30**, 359–365, 1982.
- Vennerström, S., Dayside magnetic ulf power at high latitudes: A possible long-term proxy for the solar wind velocity?, *J. Geophys. Res.*, **104**, 10,145–10,157, 1999.
- Vennerström, S., and E. Friis-Christensen, On the role of IMF by in generating the electric-field responsible for the flow across the polar-cap, *J. Geophys. Res.*, **92**, 195–202, 1987.
- Vennerström, S., E. Friis-Christensen, O. Troshichev, and V. Andresen, Comparison between the polar-cap index, PC, and the auroral electrojet indexes AE, AL, and AU, *J. Geophys. Res.*, **96**, 101–113, 1991.
- Weigel, R., W. Horton, T. Tajima, and T. Detman, Forecasting auroral electrojet activity from solar wind input with neural networks, *Geophys. Res. Lett.*, **26**, 1353–1356, 1999.
- Weigel, R. S., D. Vassiliadis, and A. Klimas, Coupling of the solar wind to temporal fluctuations in ground magnetic fields, *Geophys. Res. Lett.*, **29**(19), 1915, doi:10.1029/2002GL014740, 2002.
- Weimer, D., Models of high-latitude electric potentials derived with a least error fit of spherical harmonic coefficients, *J. Geophys. Res.*, **100**, 19,595–19,607, 1995.
- Weimer, D., A flexible, IMF dependent model of high-latitude electric potentials having "space weather" applications, *Geophys. Res. Lett.*, **23**, 2549–2552, 1996.
- Winglee, R., V. Papitashvili, and D. Weimer, Comparison of the high-latitude ionospheric electrodynamics inferred from global simulations and semiempirical models for the january 1992 GEM campaign, *J. Geophys. Res.*, **102**, 26,961–26,977, 1997.
- Wu, J. G., and H. Lundstedt, Neural network modeling of solar wind magnetosphere interaction, *J. Geophys. Res.*, **102**, 14,457–14,466, 1997.

A. J. Klimas and D. Vassiliadis, NASA Goddard Space Flight Center, Greenbelt, MD 20771, USA. (alex.klimas@nasa.gov; vassi@electra.gsfc.nasa.gov)

R. S. Weigel, Laboratory for Atmospheric and Space Physics, Boulder, CO 80303, USA. (robert.weigel@lasp.colorado.edu)